Subtopic: Internal Combustion and Gas Turbine Engines

2019 WSSCI Fall Technical Meeting
Organized by the Western States Section of the Combustion Institute
October 14–15, 2019
Albuquerque, New Mexico

Effect of Fuel Reactivity and End-Gas Temperature on Autoignition and Flame Propagation Rate in Primary Reference Fuel Mixtures at Elevated Temperature and Pressure

Andrew Zdanowicz[1], Jeffrey Mohr[1], Jessica Tryner[1], Kara Gustafson[1], Bret Windom[1], Daniel B. Olsen[1], Gregory Hampson[2] and Anthony J. Marchese[1,]*

[1]*Department of Mechanical Engineering, Colorado State University, Fort Collins, CO, USA*

[2]*Woodward Inc., Loveland, CO, USA*

[*]*Corresponding Author Email: Anthony.Marchese@colostate.edu*

Abstract: Knock in spark-ignited (SI) engines is initiated by autoignition in the unburned gases upstream of spark-ignited, propagating, turbulent premixed flames. In this study, knock propensity of SI fuels was quantified via observations of end-gas autoignition (EGAI) in unburned gases upstream of laser-ignited, premixed flames at elevated pressures and temperatures in a rapid compression machine. Stoichiometric primary reference fuel (n-heptane/isooctane) blends of varying reactivity were ignited using an Nd:YAG laser over a range of compressed temperatures and pressures, all in excess of 691 K and 18.8 bar. High-speed pressure measurements and schlieren images indicated the presence of EGAI in the unburned gases upstream of spherical, outwardly propagating flames. The fraction of the total heat release attributed to EGAI was found to vary with fuel reactivity and the time-integrated temperature of the end-gas prior to ignition. Flame propagation rates, measured using schlieren imaging, did not vary strongly with fuel reactivity but were affected by turbulence caused by variation in piston timing. Under conditions of low turbulence, measured flame propagation rates agreed with one-dimensional premixed laminar flame speed computations performed at the same conditions.

Keywords: End-Gas Autoignition, Engine Knock, Rapid Compression Machine

1. Introduction

The conventional quantification metrics for the propensity of a spark-ignited (SI) fuel to autoignite are the research and motor octane numbers (RON and MON) [1–3]. The RON and MON standards represent a fuel's resistance to knock through a comparison of the test fuel's critical compression ratio to that of a primary reference fuel blend (n-heptane and isooctane) under standardized operating conditions in a Cooperative Fuels Research (CFR) engine. Making such a comparison inherently requires large quantities of test fuel, as the engine must be run through thousands of cycles over the course of the measurement period.

Efforts to produce novel fuels (e.g., advanced biofuels), often yield very small, costly quantities however, and little is known about pertinent combustion properties in early development stages. Measurement of the fuel's octane number at this point can be impractical if not prohibitively expensive due to the quantity of fuel required. Benchtop cetane number (CN) measurement instruments, like the ignition quality tester (IQT) and the fuel ignition tester (FIT) [4,5] address these problems directly by moving away from conventional engine testing and measuring the ignition characteristics of compression-ignition (CI) fuels via alternative methods. However, an equivalent standardized benchtop instrument for measuring the ON of SI fuels has yet to be developed [6–9].

We propose that a rapid compression machine (RCM) capable of facilitating SI conditions could serve as that instrument. The ideal autoignition propensity measurement device would: (1) require small amounts of fuel for testing, (2) allow for variable end-gas conditions (e.g., pressure, temperature, species consistent with exhaust gas

recirculation), (3) include high-speed pressure measurement for apparent heat release rate calculations, (4) include optical access for flame speed measurements and EGAI observation, and (5) be amenable to chemically reacting flow modeling with detailed chemical kinetics.

An RCM has several advantages as an instrument for studying EGAI and knock propensity as proposed. Specifically, as described below, the RCM at Colorado State University has the following attributes: (1) it can safely reach a variety of temperatures and pressures consistent with end-gas conditions in current and future engines, (2) requires substantially less fuel than engine testing (~0.25 mL/RCM test), (3) is optically accessible, and (4) can be more accurately modeled than an internal combustion engine because of precise knowledge of the initial conditions and the absence of turbulent flow [1,10].

The goal of the present study is to advance methods for quantifying the knock propensity of SI fuels via observations of EGAI in unburned gases upstream of laser-ignited, premixed flames at elevated pressures and temperatures in an RCM. Primary reference fuel (PRF; n-heptane/isooctane) blends of varying reactivity ($50 \leq PRF \leq 100$) were ignited by a laser spark initiated along the centerline of the combustion chamber. High-speed pressure measurements and Schlieren imaging were used to characterize the combustion processes, approximate flame speed, and quantify the magnitude of potential EGAI events.

2. Methods

2.1 RCM – Instrumentation, Mixture Formation, and TDC Condition Control

Colorado State University's rapid compression machine (CSU RCM; pictured in Fig. 1(a)) was used to measure EGAI propensities and flame propagation rates of liquid test fuels at elevated temperatures and pressures. A 1064 nm, Q-switched, Nd:YAG laser served as the ignition source – creating a spark at the center of the combustion chamber at a prescribed delay period (e.g., 10 ms) after compression. Schlieren imaging and high-speed pressure measurements were used in combination to make observations of the resulting combustion phenomena. The optical layout for laser ignition and Schlieren imaging systems are shown in Fig. 1(b).

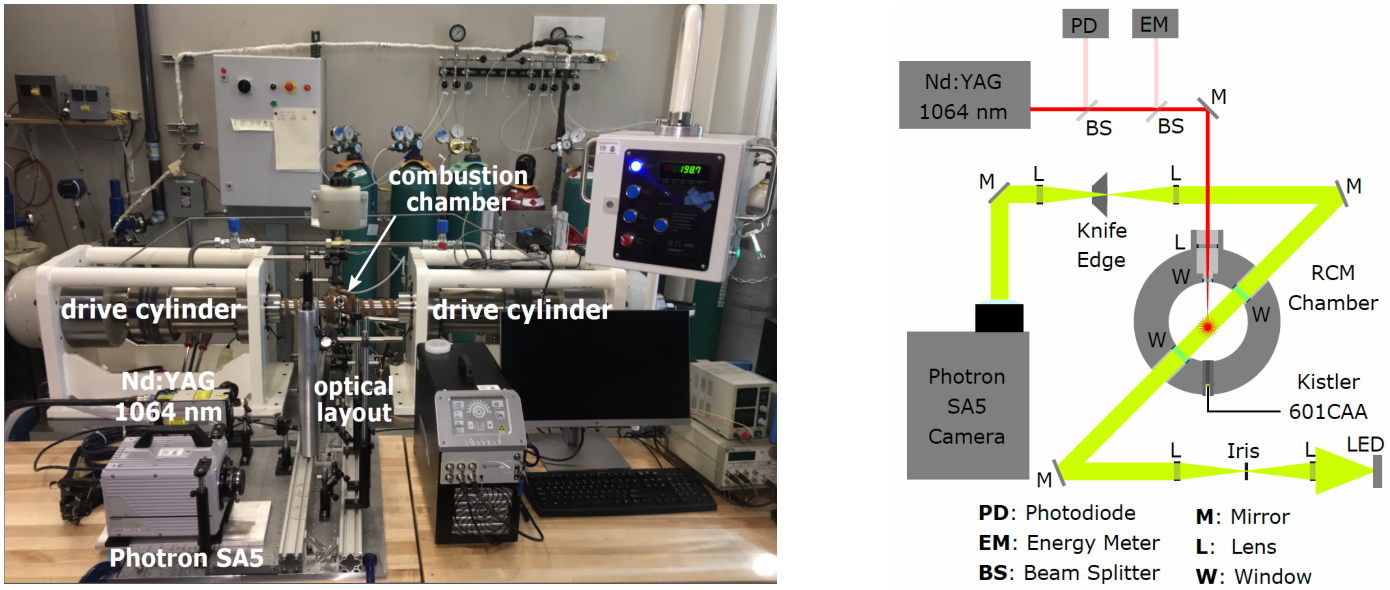

Figure 1. (a) Picture of the CSU RCM and its associated equipment. **(b)** Diagram of the RCM's optical layout. Schlieren collimated light pathway shown in green. Nd:YAG 1064 nm laser pathway shown in red.

Blends of the primary reference fuels isooctane and n-heptane were used to facilitate testing of the measurement methods over a wide range of test fuel ON. Proportioned liquid fuel blends, as designated by PRF number (e.g., PRF 80; 80% isooctane and 20% n-heptane by mole), were injected into a separate evacuated mixing tank, where they evaporated, and were then mixed with the inert and oxidizing gases. Gases were added to the tank in

succession, proportioned by their partial pressure and tank temperature. All experiments were performed with mixture components in stoichiometric proportion. External tank heaters were set to 42 ˚C to prevent condensation and an internal stir bar was used to mix the gases for a minimum of 2 hours prior to filling the RCM combustion chamber.

The initial external RCM chamber temperature was maintained at 300 +/- 2 K for all experiments. The thermodynamic conditions after compression were controlled by adjusting the initial pressure and/or varying the ratio of specific heats of the test gas mixture by varying the inert gas blend. Specifically, an inert blend of nitrogen and carbon dioxide was used to lower the ratio of specific heats of the test gas blend. The oxidizer/inert gas blends and initial pressures investigated were designated by experiment index, as listed in Table 1.

Table 1. The six test conditions used in this study. Physical changes were made to the combustion chamber fill valve during the tests performed under experiment index 5. These changes increased the compression ratio from 11.6:1 to 11.9:1. Initial pressure was lowered to achieve similar TDC conditions to those of experiment index 4.

Index	Initial Pressure	Oxidizer/Inert Blend Composition (mole %)			Compression Ratio	TDC Temp. Range	TDC Press. Range
	(bar)	O_2	N_2	CO_2	(-)	(K)	(bar)
1	1.000 ± 0.001	21%	79%	-	11.6:1	729 - 887	24.9 - 27.8
2	0.900 ± 0.001	21%	79%	-	11.6:1	730 - 867	22.7 - 25.7
3	0.750 ± 0.001	21%	79%	-	11.6:1	725 - 873	18.8 - 22.9
4	1.000 ± 0.001	21%	67.1%	11.9%	11.6:1	698 - 829	24.4 - 26.2
5	0.975 ± 0.075	21%	67.1%	11.9%	11.9:1	702 - 817	24.5 - 25.8
6	1.000 ± 0.001	21%	39.5%	39.5%	11.6:1	691 - 775	23.2 - 24.4

The top dead center (TDC) temperatures and pressures listed in Table 1 represent the full range of experimental observations for the specified initial conditions. Variation in TDC temperature and pressure was a result of variability in compression speed and asymmetry of piston timing. Fluid dynamic and thermodynamic conditions at TDC were found to be sensitive to this "piston offset." Addressing this sensitivity, experimental trials were categorized by their estimated TDC conditions, rather than their initial conditions. Specifically, trials were categorized by their piston offset and time-integrated temperature. Briefly, the time-integrated temperature (Θ) was evaluated by integrating, with respect to time, the calculated bulk mean temperature of the gases in the combustion chamber during the 10 ms interval prior to spark ignition:

$$\Theta = \int_{-10\ ms}^{0} T_m dt \tag{1}$$

where T_m is the calculated bulk-mean temperature in K and t is the time in s. The temperature history during the compression process (up to and including TDC) was estimated using the ideal gas law with the known gas composition, the initial temperature, the pressure versus time data, and the specific volume versus time data. As discussed below, the piston offset affected the convective flow field into which the flames propagated and the time-integrated temperature was known to correlate with the chemical kinetic induction period of the end-gas [11].

2.2 AHRR and EGAI Fraction Evaluation

The high-speed pressure data were used to calculate the apparent heat release rate (AHRR), in W, during the constant-volume combustion event as shown in Eq. (2) [12]:

$$AHRR = \frac{dQ}{dt} = \frac{1}{\gamma - 1} V \frac{dP}{dt} \tag{2}$$

where V is the gas volume after compression in m^3, γ is the ratio of specific heats of the mixture, P is the pressure in Pa, and t is the time in s. Note that dQ/dt represents the net rate of external heat addition to the gases in the combustion chamber that would result in the measured pressure rise dP/dt due to conversion of chemical energy to thermal energy in a homogeneous chemically reacting system. The specific heat ratio of the mixture varied over the course of each experiment and was calculated at each sample point as a function of the estimated temperature and initial mixture composition, using empirical correlations for the mixture constituents [13]. Changes in species concentrations during combustion were not accounted for.

An example AHRR profile is shown in Fig. 4 (a) to illustrate the procedures used to identify the combustion mode and quantify the fraction of the total apparent heat release attributed to the EGAI event. Distinct combustion modes—propagating flame, low-temperature heat release in the end-gas, and end-gas autoignition—were identified by their AHRR signatures. The contribution of the EGAI event to the total apparent heat release was isolated by deconvolution of the AHRR curve. A quadratic function was fit to the data before and after the EGAI peak to estimate the portions of heat release attributed to the propagating flame and the EGAI event. The heat release during EGAI was evaluated as the integral of the isolated EGAI AHRR profile (i.e., the area between the AHRR curve and quadratic fit function).

We defined the EGAI heat release fraction (f_{EGAI}) as follows:

$$f_{EGAI} = \left[\int \frac{dQ}{dt}\right]_{EGAI} \Big/ \left[\int \frac{dQ}{dt}\right]_{Total} \tag{3}$$

where dQ/dt is the apparent heat release rate in W. The numerator represents the integrated apparent heat release during EGAI in J, and the denominator the total integrated apparent heat release in J.

2.3. Estimation of Flame Propagation Rate

Schlieren images, collected in sequence, were used to measure the projected flame area for each image, which yielded an equivalent flame radius as a function of time. A second-order polynomial was fit to the equivalent flame radius versus time and flame stretch effects were eliminated through the non-linear extrapolation of Kelley and Law [14,15] to yield the zero-stretch flame speed with respect to the burned gases according to Eq. (4):

$$s_b = s_b^0 t + c r_f + 2 L_b \ln(r_f) - 4 \frac{L_b^2}{r_f} - \frac{8}{3} \frac{L_b^3}{r_f} \tag{4}$$

where s_b is the burned propagation rate approximated with the second-order polynomial in cm/s, s_b^0 is the zero-stretch burned propagation rate to be found in cm/s, t is time in s, c is a measurement constant, r_f is the equivalent spherical flame radius in cm, and L_b is the Markstein length in cm. The extrapolated zero-stretch burned propagation rate was then converted to an unburned propagation rate by correcting for the change in density across the flame front using equation Eq. (5) [15].

$$s_u = s_b \left(\frac{\rho_b}{\rho_u}\right) \tag{5}$$

where s is the flame propagation rate in cm/s, ρ is the region density in kg/m^3, and the u and b subscripts represent the unburned and burned regions across the flame respectively. Unburned density was calculated using the initial pressure and known compression ratio. Burned density was approximated using the ideal gas law and the burned

temperatures and molecular weight of the combustion products as predicted by 1-D CHEMKIN flame speed simulations with reduced chemical kinetics [16].

3. Results and Discussion

3.1. Pressure, Apparent Heat Release Rate, and End-Gas Autoignition Fraction Measurements

The TDC thermodynamic conditions (as indicated by the time-integrated temperature) and fluid dynamic conditions (as indicated by the piston offset) for the full data set are shown in Fig. 2. Although turbulence intensity was not quantified, schlieren images clearly indicated that experiments with larger piston offset had increased convective velocity in the flow field after TDC. However, the data in Fig. 2 indicate that the time-integrated temperature did not correlate with piston offset. In the discussions that follow, time-indicated temperature, piston offset, and octane number are taken to be the independent variables to which the dependent variables (e.g. f_{EGAI}, flame propagation rate) are compared.

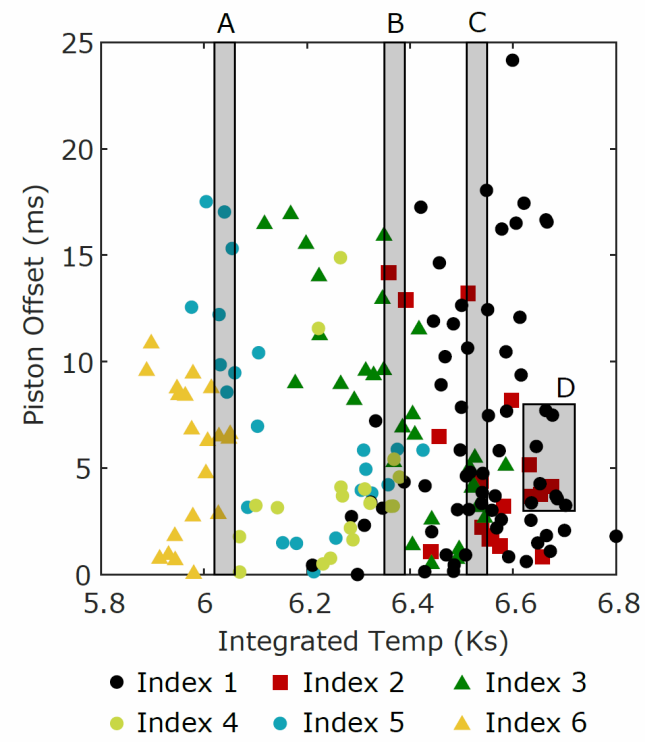

Figure 2. The TDC conditions of the entire data set, as represented by the time-integrated temperature and piston timing offset of the compression events. Different symbols correspond to the initial condition indices listed in Table 1. Each data point represents a single experiment. All of the fuel blends are included in the figure. Time-integrated temperature indicates the temperature history after compression and prior to ignition. The A, B, C, and D shaded regions illustrate the TDC conditions selected for the data presented in Figs. 3-4. Data points that fall within the shaded regions meet the selection criteria and are said to have been subjected to similar conditions upon compression.

Data point proximity in Fig. 2 indicates the similarity of the time-integrated temperature and fluid motion conditions between experiments. In the discussion that follows, four separate regions—A, B, C, and D—were arbitrarily selected to capture data points with similar TDC conditions that spanned the full range of tested fuel reactivity. Regions A, B, and C were selected to capture the effects of variation in time-integrated end-gas temperature on the laser-ignited RCM experiments. Region D was selected to maintain similar thermodynamic and fluid dynamic conditions while investigating the effect of changing fuel reactivity on combustion phenomena.

AHRR results for the PRF 100 experiments with time-integrated temperature of 6.04 ± 0.02 Ks, 6.37 ± 0.02 Ks, and 6.53 ± 0.02 Ks (i.e. regions A, B, and C in Fig. 2) are plotted in Fig. 3 (a). The magnitude of the maximum AHRR for the PRF 100 fuel blend increased substantially with the time integrated temperature as expected. The lower time-integrated temperature experiments of Region A feature much longer combustion durations with no discernable EGAI signatures. The higher time-integrated temperature experiments of Regions B and C exhibit a period of moderate AHRR followed by a dramatic change in the slope. Such behavior is indicative of an initial period in which heat release was produced by the spark-initiated propagating flame, which compressed the upstream unburned end-gases, and subsequently triggered EGAI.

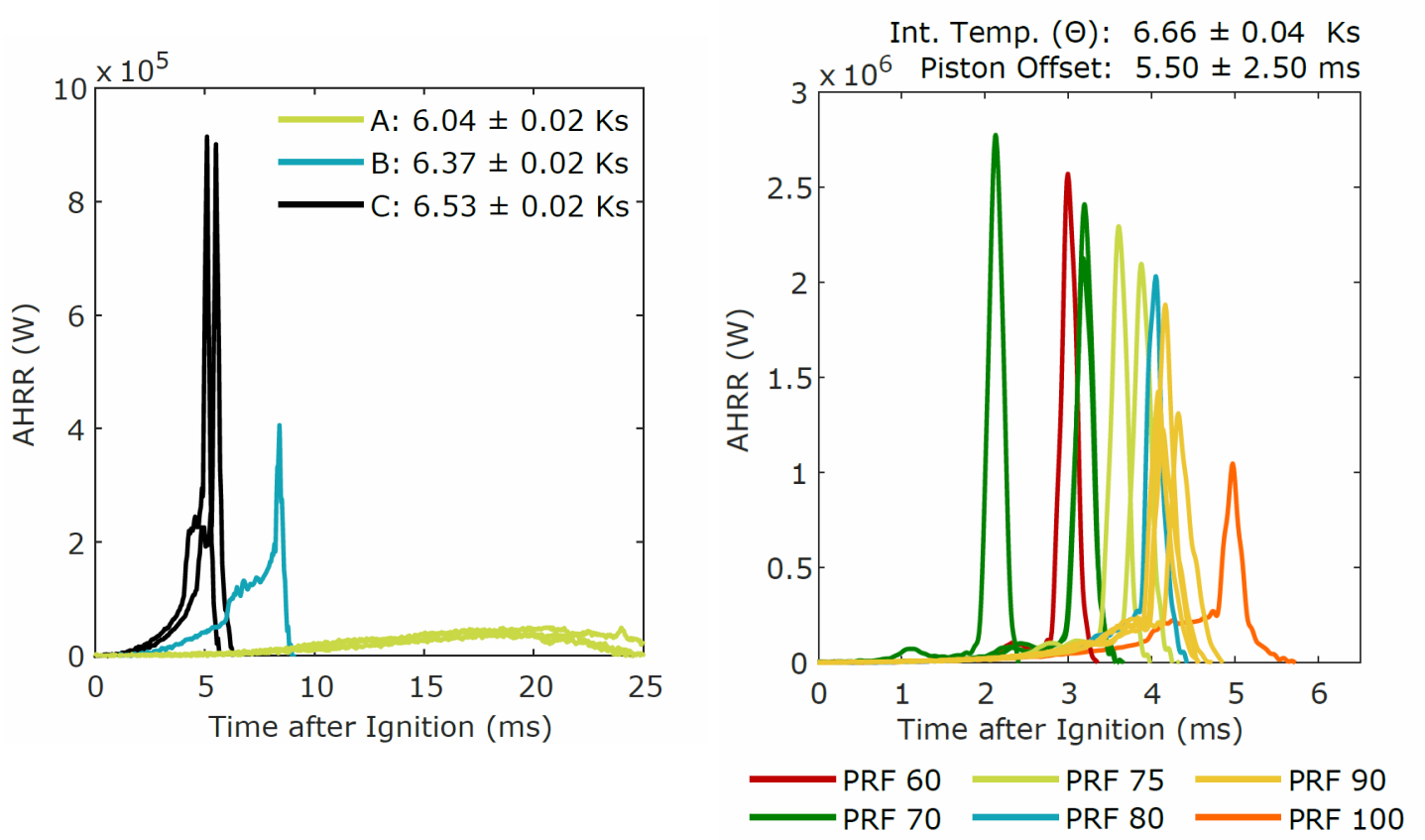

Figure 3. (a) AHRR profiles for PRF 100 experiments featuring time-integrated temperatures of 6.04 ± 0.02 Ks, 6.37 ± 0.02 Ks, and 6.53 ± 0.02 Ks (regions A, B, and C in Fig. 2). All replicate trials for all initial condition indices are shown. **(b)** AHRR profiles of experiments featuring time-integrated temperatures of 6.66 ± 0.04 Ks and piston offsets of 5.50 ± 2.50 ms (region D in Fig. 2). The colors of the AHRR curves indicate the octane number. All replicate trials within the selected range of time-integrated temperature and piston offset are included.

The flame propagation rate, and therefore EGAI timing, was dependent on the flow field conditions at TDC caused by variation in piston timing offset. Region D of Fig. 2 includes selection criteria for both time-integrated temperature and piston offset to facilitate comparison of the combustion characteristics of fuels with varying ON. AHRR profiles of experiments with time-integrated temperatures of 6.66 ± 0.04 Ks and piston offsets of 5.50 ± 2.50 ms (i.e. Region D in Fig. 2) are plotted in Fig. 3 (b). For a given level of fluid motion at TDC and time-integrated end-gas temperature, the delay between spark-ignition and EGAI decreased and the magnitude of the EGAI event increased as ON decreased. As fuel reactivity increased (with decreasing ON), the chemical kinetic induction period in the end-gas decreased, which resulted in earlier EGAI, a larger volume of autoignited gas and, therefore, a higher magnitude in apparent heat release during the EGAI event.

3.2 End-Gas Autoignition Evaluation

The characteristic AHRR behaviors that indicate the separate combustion modes are further described by the representative PRF 90, 527 K AHRR profile in Fig. 4 (a). Here, the intermediary ramp up of AHRR prior to EGAI is likely caused by a local secondary ignition site separate from the propagating flame, as there is little perceivable decrease in AHRR prior to EGAI. This hypothesis is also supported by the Schlieren images gathered for this trial, in which a turbulent flame appears to substantiate separate from the primary propagating flame. Also included in Fig. 4 (a) is a graphical representation of the f_{EGAI} metric as defined above in equation (2). The f_{EGAI} metric quantifies the fraction of the total energy released by the EGAI event. To isolate the AHRR contribution of the EGAI event, a quadratic function is fit to the AHRR profile before and after EGAI. The AHRR profile is thus deconvoluted into two heat release profiles (that of the propagating flame and of the EGAI event), which combine to form the measured total AHRR at any given time. The f_{EGAI} metric is evaluated as the integral of the isolated EGAI AHRR profile – i.e. the area below the AHRR curve and above the quadratic fit function.

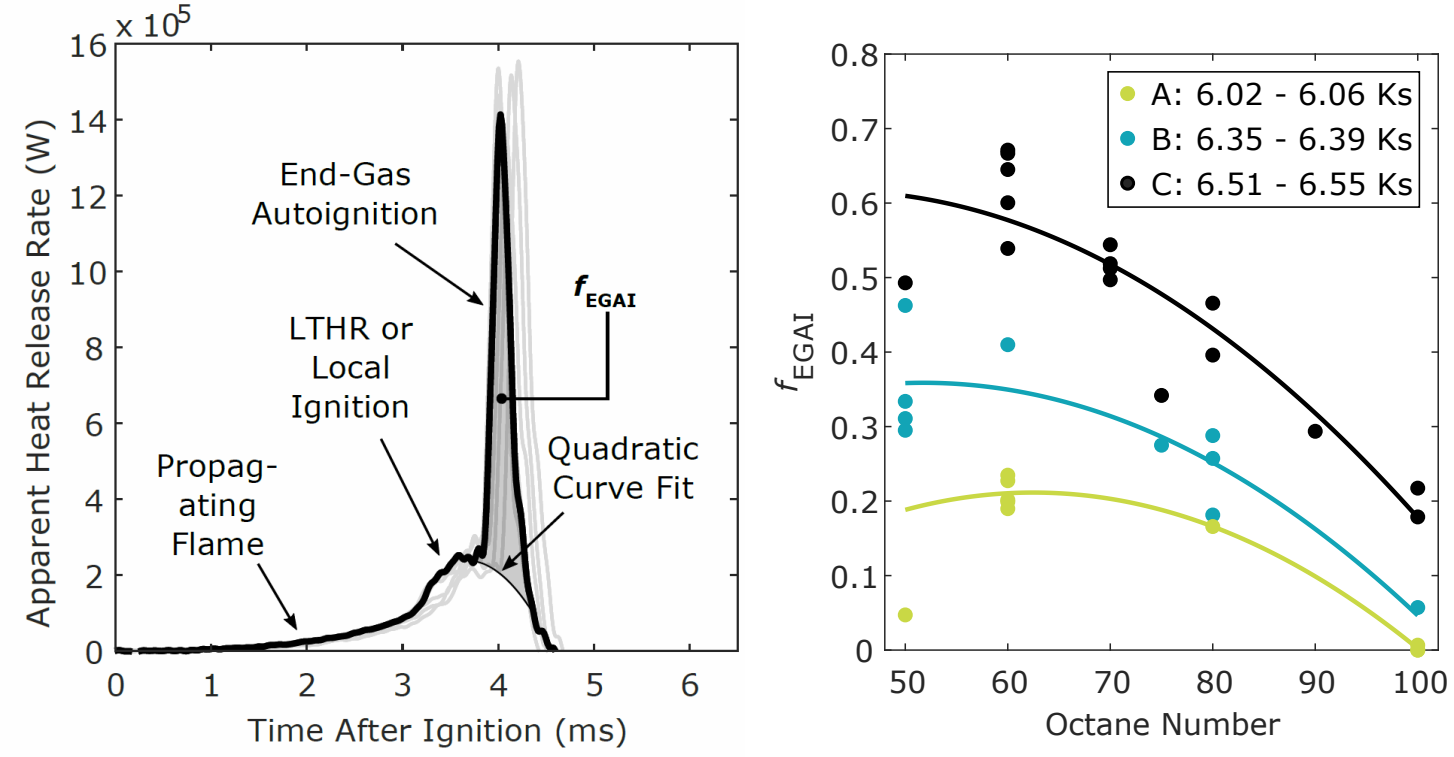

Figure 4. (a) Apparent heat release rate data derived from the raw pressure data for a PRF 90 fuel blend under experiment index 1 of Table 1. A quadratic curve fit is calculated with the AHRR data before and after the EGAI peak and approximates the amount of energy released by the propagating flame at that time. The fractional EGAI is represented by the shaded region between the AHRR profile and the quadratic fit line. **(b)** EGAI fraction (f_{EGAI}) measurements plotted against ON for $\Theta = 6.04 \pm 0.02$ Ks, 6.37 ± 0.02 Ks and 6.53 ± 0.02 Ks and all piston offsets (i.e. regions A, B, and C in Fig. 2). Each symbol represents an individual test replicate. Second order polynomials fit to the data using the least squares method.

Figure 4 (b) includes the end-gas autoignition fraction, f_{EGAI}, for all experiments with time-integrated temperature of 6.04 ± 0.02 Ks, 6.37 ± 0.02 Ks, and 6.53 ± 0.02 Ks, respectively (i.e. Regions A, B and C in Fig. 2). The fraction of the total apparent heat release attributed to EGAI was lower for experiments with lower time-integrated temperature and lower fuel reactivity (i.e., higher ON). Piston offset did not strongly influence f_{EGAI} despite its direct correlation with flame propagation rate (see §3.4). The magnitude of an EGAI event is determined by the outcome of a competition between the propagation rate of the premixed flame and the chemical kinetic induction period for the autoignition chemistry in the end-gas. The amount of reactants that the propagating flame can consume prior to EGAI decreases as the autoignition delay period decreases. One might expect a larger piston

offset and higher flame propagation rate to result in a lower f_{EGAI}. However, the end-gases are also compressed and heated by the approaching flame. As a result, a higher flame propagation rate leads to higher temperatures and reaction rates in the end-gas (which decrease the autoignition delay period), which promotes EGAI and diminishes the correlation between propagation rate and f_{EGAI}.

The magnitude of the EGAI fraction is also governed by the complexities of low temperature chemical kinetics in the end-gas. Specifically, the PRF blends tested in this study clearly exhibited low temperature heat release and negative temperature coefficient (NTC) behavior, resulting in two-stage ignition behavior as evidenced by local peaks in AHRR prior to the primary EGAI peak. This behavior is most clearly depicted in the AHRR profiles of the higher reactivity blends in Fig. 3 (b). The competition between the propagation rate of the premixed flame and chemical kinetic induction period of the end-gas subject to NTC chemistry can also result in the peculiar result of fuels with higher reactivity (e.g. PRF 50) exhibiting lower EGAI fraction for cases in which the flame fully traverses the end-gas during the NTC period. This situation might explain the observed decreases in EGAI for PRF50 in Fig. 4 (b).

In principle, the upper limit of the f_{EGAI} metric is 1.0, which would constitute homogeneous charge compression ignition (HCCI; or very rapid spark-initiated HCCI) of the entire fuel/air mixture. However, it should be noted that fuels that exhibit two-stage ignition behavior can never achieve an EGAI fraction of 1.0 because a finite fraction of the fuel is consumed by the first-state low temperature heat release. For all fuels and time-integrated temperature conditions considered in this study (experimentally and computationally), the highest value of f_{EGAI} observed was 0.70.

3.3 Combustion Observations via Schlieren Imaging

Figure 5 (a) presents select Schlieren images from a PRF 90 trial under experiment index 3. The images are mapped to the corresponding AHRR profile in Figure 5 (b). Images were recorded at 50,000 fps using a Photron SA5 high speed camera.

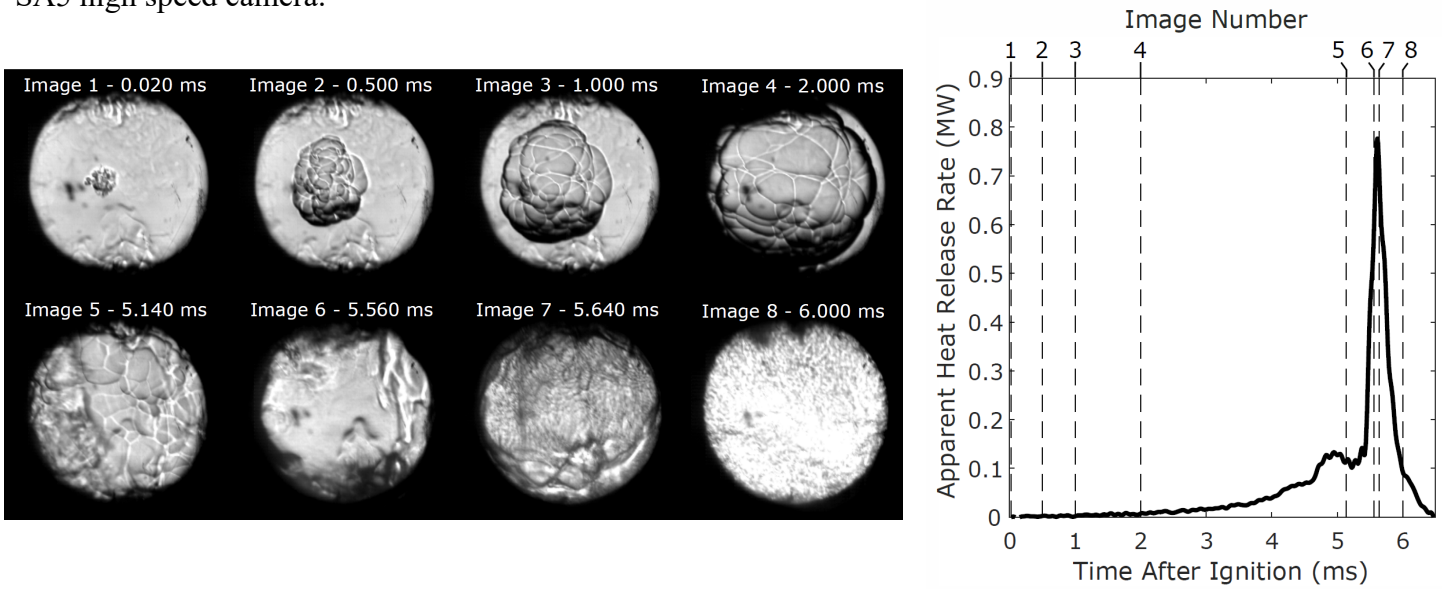

Figure 5. (a) Schlieren images captured at 50,000 frames per second for a PRF 90 fuel blend under experiment index 3. Image numbers correspond with those represented in the AHRR profile alongside. The time listed at which the image was recorded is relative to the ignition timing. **(b)** AHRR profile for images presented. Vertical dashed lines indicate the times at which those images were taken.

The first four images clearly depict early stage flame propagation. Ignition is captured just after the spark is introduced in Image 1 and the flame kernel grows outward in the subsequent images, extending beyond the field of view in Image 4. Note that the field of view is limited by the relative size of the windows to the size of the combustion chamber. By the time the flame reaches the field of view boundary, it encompasses a mere 7% of the

total chamber volume. Beyond this point, growth of cellular instabilities on the outer surface of the flame provide evidence for continued propagation between 2.0 and 4.5 ms. Then, a low magnitude spike in AHRR is detected and shortly after a secondary, more turbulent flame appears in the field of view on the left hand side (image 5). This secondary flame may be acting in conjunction with a LTHR event, as the AHRR seems to decreases momentarily before the EGAI peak. Shortly thereafter, a sudden vivid change in the view port suggests autoignition in Image 6. The cellular instabilities that were used to identify the flame front disappear, replaced by what looks to be a more uniform, homogenous gas that directly corresponds to the primary EGAI peak in the AHRR graph.

3.3 Flame Propagation Rate Measurements and EGAI Sensitivity

Flame propagation rate measurements for index 1 experiments that featured piston offsets of less than 5.00 ms are listed in Table 2 with their corresponding measured pressures and estimated temperatures at the time of ignition. Only experiments conducted using a single set of initial conditions (index 1) are presented to eliminate the effects of changing inert composition and gas density on diffusivity and propagation rates.

Table 2. Unburned flame propagation rate measurements listed by their mean and standard deviations for the index 1 experiments (initial conditions: 300 K and 1.000 bar; oxidizer/inert molar composition: 21% O_2 / 79% N_2; stoichiometric). Only the experiments with piston offsets of less than 5.00 ms are included to ensure that the effect of turbulence is minimized. The number of measurements is included to indicate the level of confidence in the data. The "Simulated LFS" column features the predicted laminar flame speeds from the 1-D CHEMKIN simulations with 590 K and 22.5 bar ambient conditions.

PRF	# of Data Points	Temp. (K)	Pressure (bar)	Measured Prop. Rate (cm/s)		Simulated LFS (cm/s)
				Mean	SD	(590 K, 22.5 bar)
50	6	571 ± 2	22.0 ± 0.2	63.3	15.0	52.5
60	4	598 ± 5	22.9 ± 0.2	80.3	6.3	51.1
70	1	614	23.8	83.5	-	50.4
75	4	605 ± 4	23.1 ± 0.2	62.5	4.1	50.2
80	3	591 ± 1	22.6 ± 0.0	65.1	10.5	49.7
90	3	612 ± 3	23.2 ± 0.1	63.3	13.9	49.2
100	5	589 ± 3	22.5 ± 0.2	65.1	8.3	48.5

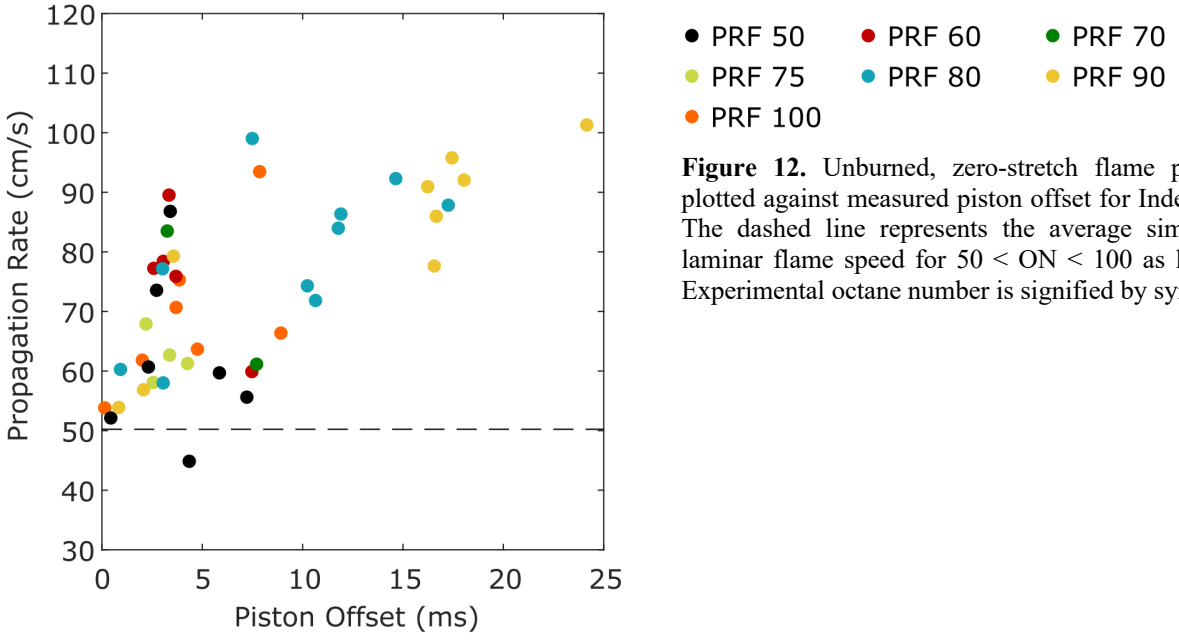

Figure 12. Unburned, zero-stretch flame propagation rates plotted against measured piston offset for Index 1 experiments. The dashed line represents the average simulated premixed laminar flame speed for 50 < ON < 100 as listed in Table 2. Experimental octane number is signified by symbol color.

Propagation rate was correlated most strongly with piston offset (Spearman rank correlation coefficient, ρ = 0.621), as depicted in Fig. 6. Propagation rate was not as strongly correlated with temperature at ignition (ρ = 0.221), pressure at ignition (ρ = 0.275), and ON (ρ = 0.239) over the ranges tested. It should be noted that the premixed laminar flame speed was not expected to vary strongly with octane number for PRF fuels for fixed upstream conditions as indicated by the simulated results listed in Table 2. The experimental results were consistent with these expectations. Moreover, as shown in Fig. 6, the measured propagation rates approached the calculated 1-D laminar flame speed predictions as piston offset approached 0.0 ms. This result (a) suggests that experimental trials with low piston offset featured quiescent post-compression flow-fields that near-laminar flames and (b) illustrates the potential of the experimental methods described herein as a means to measure flame propagation rates at elevated pressures and elevated unburned gas temperatures for experimental trials with near-symmetric compression.

4. Conclusions

The development of future fuels with reactivity behavior that deviates from that of alkanes, as well as the evolution of engines that operate beyond the conditions commensurate with RON/MON, require development of new methods to characterize fuel reactivity and knock propensity. Specifically, fuel reactivity measurement methods must be developed that enable a wide variation in end-gas conditions (pressure, temperature, and speciation), incorporate advanced diagnostics to elucidate the onset of EGAI, require small quantities of fuel, and are amenable to comparisons against computational modeling with detailed chemical kinetics.

The results of this study demonstrate the ability to evaluate knock propensity of SI fuels by observation of EGAI in the unburned gases upstream of laser-ignited, premixed flames at engine-relevant pressures and temperatures in an RCM. To demonstrate this principle, stoichiometric PRF blends of varying reactivity ($50 \leq PRF \leq 100$) were ignited at five discrete temperature and pressure conditions, all in excess of 691K and 18.8 bar, which produced outwardly propagating, laminar premixed flames. High-speed pressure measurements, paired with Schlieren imaging, clearly indicated the presence of EGAI for PRF blends. The magnitude of the EGAI event, as quantified by the fraction of the total heat release occurring during EGAI, varied inversely with octane number. Future work will focus on testing a wider range of fuels, quantifying the effects of EGAI heat release fraction on overall combustion efficiency, and defining reactivity metrics that are not anchored to a comparison with primary reference fuels.

5. Acknowledgements

This work was funded by Department of Energy (DOE) award DE-EE0008331.

6. References

[1] Z. Wang, H. Liu, R.D. Reitz, Knocking combustion in spark-ignition engines, Progress in Energy and Combustion Science. 61 (2017) 78–112. doi:10.1016/j.pecs.2017.03.004.
[2] ASTM D2700-12: Standard Test Method for Motor Octane Number of Spark-Ignition Engine Fuel, (2018).
[3] ASTM D2699-12: Standard Test Method for Research Octane Number of Spark-Ignition Engine Fuel, (2018).
[4] D02 Committee, Test Method for Determination of Derived Cetane Number (DCN) of Diesel Fuel OilsIgnition Delay and Combustion Delay Using a Constant Volume Combustion Chamber Method, ASTM International, n.d. doi:10.1520/D7668-17.
[5] D02 Committee, Test Method for Determination of Ignition Delay and Derived Cetane Number (DCN) of Diesel Fuel Oils by Combustion in a Constant Volume Chamber, ASTM International, n.d. doi:10.1520/D6890-16E02.

[6] D02 Committee, Test Method for Determination of Octane Number of Spark-Ignition Engine Fuels by On-Line Direct Comparison Technique, ASTM International, n.d. doi:10.1520/D2885-13.
[7] V.N. Korolev, A.V. Marugin, Determination of the octane number of a fuel by the IR spectroscopy method, Journal of Applied Spectroscopy. 67 (2000) 336–342. doi:10.1007/BF02681855.
[8] S. Gersen, M. van Essen, H. Levinsky, G. van Dijk, Characterizing Gaseous Fuels for Their Knock Resistance based on the Chemical and Physical Properties of the Fuel, SAE International Journal of Fuels and Lubricants. 9 (2016) 1–13. doi:10.4271/2015-01-9077.
[9] S. Gersen, M.H. Rotink, G.H.J. Van Dijk, H. Levinsky, A new experimentally tested method to classify gaseous fuels for knock resistance based on the chemical and physical properties of the gas, 2011.
[10] S. Bhoite, A Computational Study of Autoignition, Spark Ignition and Dual Fuel Droplet Ignition in a Rapid Compression Machine, Colorado State University, 2017.
[11] J. Livengood, P. Wu, Correlation of autoignition phenomena in internal combustion engines and rapid compression machines, Symp. (Int.) Combust. (1955) 347–356.
[12] J.B. Heywood, Internal combustion engine fundamentals, McGraw-Hill, New York, 1988.
[13] M.W. Chase, NIST-JANAF Thermochemical Tables, J. Phys. Chem. Ref. Data. Monograph 9 ` (1998) 1–1951.
[14] A.P. Kelley, C.K. Law, Nonlinear effects in the extraction of laminar flame speeds from expanding spherical flames, Combustion and Flame. 156 (2009) 1844–1851. doi:10.1016/j.combustflame.2009.04.004.
[15] C.K. Law, Combustion physics, Cambridge University Press, Cambridge ; New York, 2006.
[16] P. Pal, T. Lu, Multidimensional Numerical SImulations of Knocking Combustion in a Cooperative Fuel Research Engine, Journal of Energy Resources Technology. (2018). doi:10.1115/1.4040063.